Computers and Structures 319 (2025) 108006

Contents lists available at ScienceDirect

Computers and Structures

journal homepage: www.elsevier.com/locate/cas

Anisotropic phase-field fracture parameters: Evolutionary algorithm perspective

Tota Rakesh Kumar [a,b,*], Marco Paggi [a]

[a] Computational Mechanics Group, Research Unit MUSAM – Multi-scale Analysis of Materials, IMT School for Advanced Studies Lucca, Piazza San Francesco, 19, 55100, Lucca, Italy

[b] School of Marine Engineering and Technology, Indian Maritime University, Chennai, 600119, Tamil Nadu, India

HIGHLIGHTS

- Meta-heuristic algorithms applied to anisotropic phase-field for fracture.
- Sensitivity analysis of the phase-field parameters.
- Identification of phase-field fracture parameters.
- Most efficient metaheuristic machine learning algorithm identified.
- Epistemic uncertainty.

ARTICLE INFO

Keywords:
Anisotropic phase field approach to fracture
Metaheuristic algorithms
Inverse problems
3D printed PLA

ABSTRACT

Polylactic acid (PLA) plays a prominent role in medical implants, packaging, and the textile industry, among the various industrial sectors. Components can be efficiently 3D printed by the Fusion Deposition Modeling (FDM) process, which however is inducing a material anisotropy due to the layer-by-layer deposition. The phase field (PF) approach to fracture generalized to handle anisotropic brittle materials is herein critically examined since it offers potential capabilities to simulate crack paths in such materials. Since the formulation is based on an anisotropic structural tensor $\boldsymbol{\omega}$ with the incorporation of penalty parameter β, this governs the material fracture energy G_c, the internal length scale l_c, and the apparent strength. The novel contribution of the work lies in integrating a metaheuristic machine learning algorithm (MLA) with the PF approach to robustly estimate fracture parameters (G_c, l_c and β) and get an insight into epistemic uncertainty of the formulation. Results highlight that particle swarm optimization (PSO) is robust in estimating fracture parameters to reproduce target force-displacement response curves. Sensitivity analysis of fracture parameters reveals the critical role of β in influencing fracture predictions.

1. Introduction

In the past decade, additive manufacturing (AM), also known as 3D printing, has become a very popular field and revolutionized the manufacturing industry with supremacy over conventional processes in creating complex structures [1,2] with polymers, ceramics, metals, and also composite materials. AM has played a significant role in Industry 4.0 by reducing material waste and promoting a sustainable, cleaner production process, a subject of interest in academia and industry [3]. In this regard, different types of additive manufacturing techniques and methods have been developed and successfully implemented at the industry level, such as selective laser melting [4], selective laser sintering [5], fused filament fabrication [6], fused deposition modeling [7], direct energy deposition [8], etc. Among the above-mentioned methods, FDM is the most widely adopted technique [9] in the engineering field because the components produced by the FDM process [10] are of high quality with excellent retention of mechanical properties and also maintain good dimensional accuracy with repeatability. FDM works on the layer-by-layer concept in which the 3D-printed material is extruded from

* Corresponding author at: Computational Mechanics Group, Research Unit MUSAM – Multi-scale Analysis of Materials, IMT School for Advanced Studies Lucca, Piazza San Francesco, 19, 55100, Lucca, Italy.
Email addresses: totarakeshk@imu.ac.in (T. Rakesh Kumar), marco.paggi@imtlucca.it (M. Paggi).

https://doi.org/10.1016/j.compstruc.2025.108006
Received 10 August 2024; Accepted 13 October 2025
Available online 29 October 2025

Nomenclature

Acronyms

2D	Two-dimensional space
ABC	Ant Bee Colony
CS	Cuckoo Search
FDM	Fused Deposition Modelling
FEA	Finite Element Analysis
FEM	Finite Element Method
GA	Genetic Algorithm
MLA	Metaheuristic machine Learning Algorithm
PFF	Phase Field for Fracture
PLA	Polylactic acid
PSO	Particle Swarm Optimizaition
SENB	Single Edge Notch Bending
TLBO	Teaching Learning Based Optimization

Variable notation

$\mathbf{u}$	Displacement field vector
β	Penalty parameter
ν	Poisson ratio
$\boldsymbol{\omega}$	Anisotropic structural tensor
Φ	Phase field variable
Υ	PSO target cost function
E	Young's modulus
G_c	Fracture energy
l_c	Internal length scale parameter

a nozzle tip in a semi-solid state, deposited on a substrate, and then allowed to solidify, resulting in a solid 3D-printed part.

The mechanical strength behavior of various 3D printed polymer materials available on the market, such as acrylonitrile butadiene styrene, polylactic acid, polycarbonate, polyethylene terephthalate glycol, and polyamide, has been studied in [11,12]. Out of the polymers mentioned above, the strength and fracture analysis of 3D printed PLA material has been investigated widely since it is eco-friendly and biodegradable. PLA can also be blended with other materials to accelerate the degradation [13,14] and serve applications in automobiles [15], biomedical fields [16,17], etc. 3D printed components using the FDM method best suits for bio-degradable materials [18]. The printing process parameters such as raster orientation, layer thickness, printing speed, and extruded temperature, to name a few, need to be set optimally [19] and should be maintained consistently throughout the printing process. From the literature [12,20–22], it was found that the process parameters of 3D printed PLA parts produced by the FDM process strongly affect the mechanical and fracture strength. Even the mechanical behavior of a 3D printing material changes by altering the printing orientation [23]. This motivates the study of the mechanical and fracture strength of PLA materials concerning particular printing process parameters and, in general, the numerical investigation of the anisotropic behavior of such 3D-printed components.

The present work conducts two experimental tests on 3D-printed PLA materials. Experimental tensile tests are conducted as per ASTM standards [24] to investigate the mechanical properties [25] such as Young's modulus E, and tensile strength $\sigma_{\max}$. Single edge notch bending (SENB) experimental tests are also conducted as per ASTM standards [26] to investigate the effect of anisotropy on fracture toughness G_C [27,28]. The printing process parameters are set consistently to prepare both testing 3D printed samples. Since the PLA material in the 3D printing process is deposited layer-by-layer, the material might exhibit anisotropic behavior [19,29]. Material properties obtained from the above tests are dependent upon the 3D printing process parameters, and there might be a possibility of experience a strength reduction even higher than 50 % as compared to those traditionally manufactured by injection molding [30]. The finite element analysis (FEA) based on the phase field model for fracture (PFF) proposed in [31] is implemented in this work. The generalization to anisotropic materials closely simulates the fracture behavior of 3D-printed PLA materials. The PFF leads to LEFM predictions for a vanishing internal length scale [32], with crack evolution ruled by the Griffith criterion [33].

Since 3D printed materials experience anisotropic behavior, the anisotropic structural tensor $\boldsymbol{\omega}$ is incorporated into the crack surface density function term [34,35] of the basic isotropic PFF formulation [31]. The anisotropic tensor term contributes to the directionality of the crack evolution and consists of a penalty parameter β that significantly influences the crack orientation [36] during crack propagation. Several researchers [36–39] have studied the crack propagation phenomenon by exploiting anisotropic PFF numerical models and applying them to polycrystalline materials [40–42]. While the crack path due to anisotropic behavior has been studied intensively, how the effect of the penalty parameter β influences the global force-displacement response of the experimental results remains an open question yet to be investigated. In this study, we analyze the effect of the value β by using a parameter identification procedure with an inverse method to match the target force-displacement curve to a numerically simulated response. The material parameters E, G_c, β, l_c are identified by minimizing the user-defined cost function. In the literature, particle swarm optimization (PSO) [43] algorithm has been applied to fracture [44] and plasticity [45] problems to identify the respective model parameters, and in [46] the Bayesian approach was used to estimate the phase field model parameters. The question arises as to which metaheuristic optimization algorithm best suits isotropic and anisotropic fracture parameter identification problems. In this direction, the authors herein explore evolutionary machine learning algorithms (MLA) such as PSO [43,47], PSO-GA [48], ABC-PSO [49,50], CS [51], TLBO [52], and EJAYA [53,54]applied to isotropic PFF ($\beta = 0$) test problems, compare predictions and find the most efficient algorithm for identifying PFF parameters. Subsequently, the best obtained algorithm is applied to the proposed PFF-MLA combined approach to determine the effect of the penalty parameter β in identifying target input fracture mechanics parameters.

The overview of the paper is as follows. The numerical implementation of anisotropic PFF is outlined in Section 2. The combined PFF-MLA is outlined in Section 3, followed by Section 4, which investigates the best optimization algorithm for identifying the PFF parameters. Section 5 discusses the 3D-printed PLA material fabrication process, experimental testing methodology for tensile and SENB loading cases, and the numerical investigation of sensitivity analysis of penalty parameter β. Finally, in Section 6, results are discussed.

2. Anisotropic phase field model for fracture in a nutshell

This section provides an overview of the well-known phase field approach to fracture generalized to handle anisotropic brittle materials. The underlying concept of phase field applied to fracture emerged from the fundamental principles of Griffith's theory [33] applied to brittle materials, which states that a crack propagates when the fracture energy required to generate the new crack surface equals the amount of elastic strain energy released in the material due to crack growth. The mathematical expression of Griffith's total energy functional Π_T includes the contributions of the elastic strain energy Π_E, the fracture surface energy Π_S, and the potential energy $\mathcal{P}$ due to external loading:

$$\Pi_T := \Pi_E + \Pi_S - \mathcal{P} \tag{1}$$

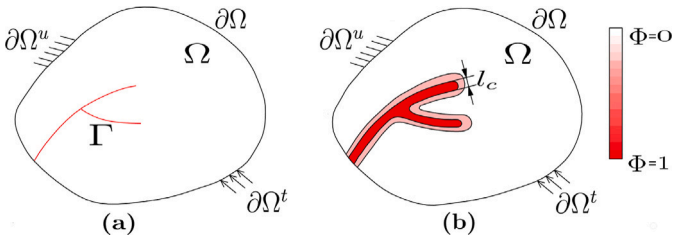

Fig. 1. (a) Schematic representation of the continuum Ω with a crack Γ and boundaries $\partial\Omega^u$, $\partial\Omega^t$. (b) Approximation of the sharp crack into a diffusive region of width l_c, where Φ denotes the phase field damage variable.

Consider a continuum domain $\Omega \subset \mathbb{R}^n$ in the reference configuration of dimension $n \in [1, 3]$ with external boundary $\partial\Omega$ and an evolving internal cracked discontinuity $\Gamma \subset \mathbb{R}^{n-1}$. The displacement field $\mathbf{u}$ is imposed on the Dirichlet boundary $\partial\Omega^u$ and surface tractions $\bar{\mathbf{t}}$ are applied on the Neumann boundary $\partial\Omega^t$, see Fig. 1, where $\partial\Omega = \partial\Omega^u \cup \partial\Omega^t$ and $\partial\Omega^u \cap \partial\Omega^t = \varnothing$. Body forces $\mathbf{b}$, if any, are applied on the continuum Ω. The total energy of the system reads:

$$\Pi_T(\mathbf{u}, \Phi) = \underbrace{\int_\Omega \Psi_E(\boldsymbol{\varepsilon}(\mathbf{u}), \Phi)\, \mathrm{d}\Omega}_{\Pi_E} + \underbrace{\int_\Gamma G_c\, d\Gamma}_{\Pi_S} \underbrace{- \int_\Omega \mathbf{b} \cdot \mathbf{u}\, \mathrm{d}\Omega - \int_{\partial\Omega^t} \bar{\mathbf{t}} \cdot \mathbf{u}\, \mathrm{d}\partial\Omega}_{\mathcal{P}} \tag{2}$$

The second term in Eq. (2) can be expressed in the regularized form [55] by approximating the sharp crack into a diffusive region with a phase field damage variable Φ as shown in Fig. 1. The value of Φ ranges between 0 and 1, with 0 representing an intact material and 1 corresponding to a fully cracked material. The regularized expression reads

$$\Pi_S(\Phi) := \int_\Gamma G_c\, d\Gamma \approx \int_\Omega G_c \gamma(\Phi, \nabla\Phi) \mathrm{d}\Omega \tag{3}$$

in which $\gamma(\Phi, \nabla\Phi)$ represents the crack surface density function that can be expressed in general form [56] as

$$\gamma(\Phi, \nabla\Phi) = \frac{1}{C_0}\left[\frac{\alpha(\Phi)}{l_c} + l_c \nabla\Phi \cdot \nabla\Phi\right] \tag{4}$$

where l_c is the regularized internal length scale parameter that governs the width of the diffusive crack. When $l_c \to 0$, the regularized crack surface Γ-converges to the sharp crack [57], satisfying the Griffith's criterion [33]. The standard Ambrosio–Tortorelli (AT-2) model [58] is adopted in the present work, and the crack geometric function $\alpha(\Phi)$ and the normalized factor C_0 in Eq. (4) are [31,59]:

$$\alpha(\Phi) = \Phi^2, C_0 = 2 \tag{5}$$

To consider the material anisotropy induced by the layer deposition in the PFF analysis, the second-order structural tensor $\boldsymbol{\omega}$ is incorporated into the nonlocal part of isotropic crack surface density for an anisotropic case as shown in Eq. (6):

$$\gamma(\Phi, \nabla\Phi) = \frac{1}{2}\left[\frac{\Phi^2}{l_c} + l_c \nabla\Phi \cdot \boldsymbol{\omega} \cdot \nabla\Phi\right] \tag{6}$$

The second-order tensor $\boldsymbol{\omega}$ is frame-invariant. The surface energy for crack propagation depends on the material orientation θ, which characterizes the anisotropic failure of the material. Following Clayton and Knap [34], $\boldsymbol{\omega}$ can be defined as

$$\boldsymbol{\omega} = \mathbb{I} + \beta(\mathbb{I} - f \otimes f), \qquad \mathbb{I} = \begin{bmatrix} 1 & 0 \\ 0 & 1 \end{bmatrix} \tag{7}$$

where $\mathbb{I}$ is a second-order identity tensor and f represents a vector normal to the material orientation plane θ. $\beta \gg 1$ represents the degree of anisotropy contributing to the crack evolution in the surface energy term Π_S along the direction of material orientation plane θ. The isotropic material behavior can be retrieved when the penalty parameter β is vanishing (orientation independent).

Therefore, the surface energy term Π_S in Eq. (2) for an anisotropic material assumes the following final form:

$$\Pi_S(\Phi) = \frac{G_c}{2}\int_\Omega \left[\frac{\Phi^2}{l_c} + l_c \nabla\Phi \cdot \boldsymbol{\omega} \cdot \nabla\Phi\right] \mathrm{d}\Omega \tag{8}$$

The elastic energy $\Psi(\boldsymbol{\varepsilon}(\mathbf{u}), \Phi)$ is split into tensile Ψ_0^+ and compressive Ψ_0^- parts, as is typically done to degrade the material response only in tension according to [31], and is controlled by the evolution of the phase field function $g(\Phi) = (1 - \Phi)^2 + \kappa_p$ with a parameter κ_p of the order of 10^{-6} to avoid ill-conditioning of the stiffness matrix when $\Phi \to 1$. The final expression reads

$$\Pi_E(\mathbf{u}, \Phi) = \int_\Omega [g(\Phi)\Psi_0^+(\boldsymbol{\varepsilon}) + \Psi_0^-(\boldsymbol{\varepsilon})] \mathrm{d}\Omega \tag{9}$$

Now, the elastic energy term Π_E in Eq. (9) and the anisotropic surface energy term Π_S in Eq. (8) are introduced into Eq. (2). The weak form of the displacement field $\mathbf{u}$ and phase field Φ is then obtained by applying the energy minimization principle to Eq. (2) with respect to the state variables ($\mathbf{u}$, Φ):

$$\frac{\partial\Pi(\mathbf{u}, \Phi)}{\partial\mathbf{u}} = \int_\Omega \boldsymbol{\sigma} \cdot \delta\boldsymbol{\varepsilon}\, \mathrm{d}\Omega - \int_\Omega \mathbf{b} \cdot \delta\mathbf{u}\, \mathrm{d}\Omega - \int_{\partial\Omega^t} \bar{\mathbf{t}} \cdot \delta\mathbf{u}\, \mathrm{d}\partial\Omega^t = 0 \tag{10a}$$

$$\frac{\partial\Pi(\mathbf{u}, \Phi)}{\partial\Phi} = \int_\Omega -2(1 - \Phi)\, \Psi_0^+(\boldsymbol{\varepsilon})\, \delta\Phi\, \mathrm{d}\Omega + \int_\Omega \frac{G_c}{2}\left[\frac{1}{l_c} 2\Phi\delta\Phi + l_c \nabla \cdot (\boldsymbol{\omega} \cdot \nabla\delta\Phi)\right] \mathrm{d}\Omega = 0 \tag{10b}$$

The Cauchy stress tensor is $\boldsymbol{\sigma} = \frac{\partial\Psi_E}{\partial\boldsymbol{\varepsilon}}$. To enforce the irreversibility of the phase field damage ($\dot{\Phi} > 0$), a history variable $\mathcal{H}$ is introduced [31], which takes the maximum strain energy value during the damage evolution process:

$$\mathcal{H} = \begin{cases} \Psi_0^+(\boldsymbol{\varepsilon}) & \text{if } \Psi_0^+(\boldsymbol{\varepsilon}) > \mathcal{H}_n \\ \mathcal{H}_n & \text{otherwise} \end{cases} \tag{11}$$

The numerical implementation of the PFF formulation into the finite element method (FEM) is performed as in [31]. The weak forms in Eq. (10) are solved using a staggered scheme to obtain the displacement $\mathbf{u}$ and the phase field Φ solutions, see [31] for more details. Both equations are connected with the history field variable in Eq. (11) to exchange the state variable during the iterative scheme.

3. Integration of metaheuristic algorithms and the phase field approach to fracture

The integration of metaheuristic machine learning algorithms and the formulation of the phase field approach to fracture is proposed to identify fracture mechanics parameters for a user-defined purpose. The issue of material parameters' identification to fulfill the desired system functionality and identify new material design solutions is a timely research topic. The optimization algorithms can tackle the inverse problems, and the metaheuristic algorithms [60], which are inspired by natural phenomena, are particularly efficient for this task. Although the metaheuristic algorithms [61,62] employ various search strategies, they typically balance local exploitation with global exploration to solve the inverse problems. The objective of local exploitation is to find better solutions in the vicinity of the current search space, while global exploration aims to find superior solutions across the complete space of

admissible solutions. This combination resolves the problems encountered by gradient-based optimization algorithms that contain only local information [45].

The metaheuristic optimization approach called PSO has been proposed and tested in [44] for the very first time in relation to the problem of parameter identification for the isotropic phase field approach to fracture, providing promising results. Here, the methodology is generalized and tested in relation to anisotropic fracture and additional metaheuristic optimization approaches based on genetic algorithms and other machine learning techniques are exploited. PSO [43] is inspired by a flock of birds' behavior in search of food, where they help each other to reach their destination by exchanging information to find the optimal solution. To increase the performance of the PSO algorithm, a velocity constriction factor-based approach [47,63] is implemented.

Alternatively, genetic algorithms (GA) [64] can be exploited for inverse analyses, mimicking the process of population evolution by using several genetic processes, including crossover, mutation, and selection, to produce a new generation within the present population and progressively move it closer to an optimal solution. The ABC algorithm [65], for instance, is based on the approach used by a swarm of honey bees to find food sources. Two distinct beehive groups exchange information to discover these sources successfully. First, there are the employee bees working and taking advantage of a food supply. Secondly, unemployed bees (scout bees) are constantly searching for a food supply. The implementation details of hybrid algorithms PSO-GA [48] and ABC-PSO [49,50] take advantage of their respective individual algorithms and solve the inverse problems. The cuckoo's brood parasitic behavior is the basis for the Cuckoo Search (CS) algorithm [51]. Lévy flights are used by CS to search the solution space and create step sizes efficiently. Switch probability is used for the local search when a specific percentage of solutions are eliminated.

The teaching-learning-based optimization algorithm (TLBO), on the other hand, is an algorithm that draws inspiration from the teaching-learning process [66,67] and is based on how a teacher's influence affects the work that students do in a class. The program simulates how a teacher and students would interact in a classroom. The population-based TLBO approach algorithm implementation details can be found in [66]. Another approach that can be used to solve the inverse problem is the Enhanced JAYA (EJAYA) algorithm [53], whose goal is to find a search mechanism that fully utilizes population data using a combination of local exploitation and global exploration tactics. A global exploration approach and a local exploitation strategy are part of the planned search mechanism, which was missing in the JAYA algorithm [68]. A detailed procedural description is found in [53].

3.1. Numerical implementation of combined PFF-MLA for parameter identification

All the above-mentioned machine learning algorithms do not rely on the gradient of the objective function, while they require the objective function to be evaluated in the hyper-parameter design space. The converged solution has to be identified by minimizing the objective function Υ. For the present mechanical problems, the cost function to be minimized can be set as the difference between the predicted and the target reaction force-displacement curves:

$$\Upsilon(\chi) = 1 - \frac{1}{n}\sum_{d=1}^{n}\sqrt{\left[\frac{\Delta Rx_d(\chi)}{\hat{Rx}_{\max}(\chi)}\right]^2}; \quad \Delta Rx_d(\chi) = Rx_\tau - Rx_s(\chi) \tag{12}$$

where:

$$\left.\begin{array}{l} Rx_s : \text{history of simulated reaction forces} \\ Rx_\tau(\chi) : \text{target value of the reaction forces} \\ \hat{Rx}_{\max}(\chi) = \max\{\max(Rx_s(\chi)), \max(Rx_\tau)\} \end{array}\right\} \text{for same imposed time steps } d = 1, \dots, n$$

Algorithm 1 Integrated phase-field fracture (PFF) - metaheuristic machine learning algorithm (MLA) for parameter identification.

```
Initialization
Input data: population size N_p, maximum number of iterations It_max, MLA algorithm tuning parameters (if required)
Output data: optimized solutions P_opt at the minimum of the cost function Υ
——— Initialization ———
for all i = 1, ..., N_p do
    Generate a population with random positions χ_i^0 in the 3D (℘ = 3) parametric space (E, G_c, l_c) within the search space.
    Evaluate cost function Υ(χ_i^0) using the phase field fracture FE model.
end for
Assign P_opt ← argmin Υ(χ_i^0)
——— Main loop of MLA algorithm ———
for k = 1, ..., It_max do
    for all i = 1, ..., N_p do
        Update solution χ_i^k based on the MLA algorithm
        if χ_i^k ∉ ℘ then
            reassign randomly χ_i^k in ℘
        end if
    end for
    P_opt ← χ_opt
end for
```

Here, $\hat{Rx}_{\max}(\chi)$ denotes the maximum value of the reaction force out of the $Rx_s(\chi), Rx_\tau$. The cost function $\Upsilon(\chi) \to 1$ if the optimization algorithm's simulated curve and the target response curve match each other. The following material properties are considered for identification: Young's modulus E, the fracture energy G_c, and the internal length scale parameter l_c. The initial population size of the variables is $N_p = 30$ and is randomly dispersed within the design-constrained space. The search space is defined in such a way as to obtain a feasible optimal parameter solution. The target force-displacement response curve for the benchmark problems is synthetically generated based on predefined material properties (E, G_c, l_c). The simulated reaction forces for each solution set are computed, and the corresponding cost function for the population size is evaluated. The solution set is then updated using the mechanism of MLA, iteratively refining the solutions until convergence to the target response of the material properties. The combined PFF-MLA pseudo-algorithm, which integrates all the various optimization algorithms, is described in Algorithm 1. For further clarity, the step-by-step numerical implementation of the PFF-MLA methodology is illustrated in the flowchart shown in Fig. 2.

4. Comparison of metaheuristic algorithm techniques applied to phase field fracture mechanics

This section aims at investigating the performance of the metaheuristic optimization algorithms when applied to inverse phase field fracture mechanics problems required to identify model parameters to match a given output response. The above-selected algorithms are compared in relation to a notched specimen tested under tensile loading (SENT) and for a single-edge notched bending (SENB) testing geometry, to evaluate their efficiency in the identification of the phase-field fracture mechanics parameters. The initial population is set to be the same for all algorithms, for the purpose of a consistent comparison. The geometry, loading, and boundary conditions of the two test problems are shown in Figs. 3 and 4, respectively. First, the isotropic case ($\beta = 0$) is examined. The target force-displacement response curves for each test are synthetically generated based on the set of parameters collected in Table 1. The set of parameters for the two test

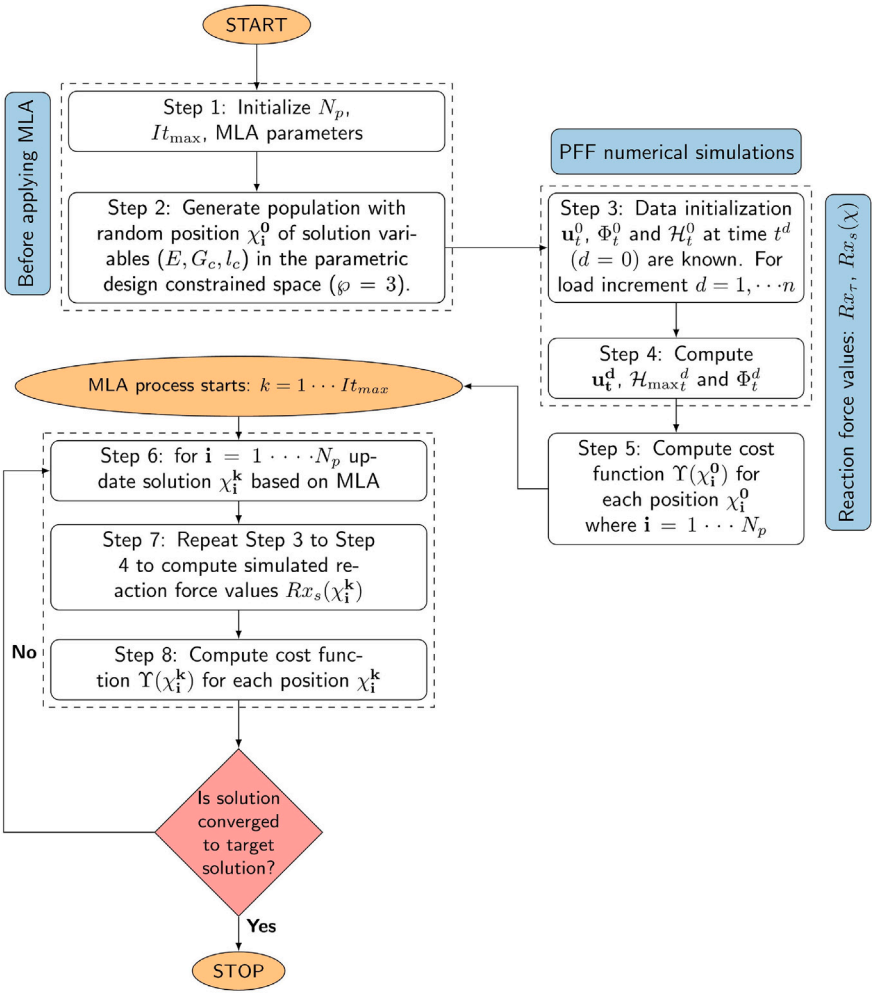

Fig. 2. Flow chart showing combined PFF-MLA for fracture mechanics parameters' identification.

problems is selected to be very different to assess the reliability of the methods in case of materials with very small or very large fracture energies. The design-constrained space is also reported in the same table.

The particles' positions within the design space at the end of the execution of the PFF-MLA algorithms (solutions corresponding to the respective minima of the cost functions) for the two test problems are shown in blue in Figs. 5 and 7, respectively.

For the first test case related to the edge-notched specimen under tensile loading (Fig. 5), the values to be identified from the virtual experiment are $E = 210$ GPa, $G_c = 2.7$ kN/mm, $l_c = 0.1$ mm and are shown with a red star in the figures. They were closely matched by the PSO algorithm, see Fig. 5(a). The PSO-GA and the ABC-PSO algorithms almost converged to the optimal solution, although not exactly matching the target (Fig. 5(b) and (c)). The CS algorithm did not converge to the target solution (Fig. 5(d)) because the variables were trapped within their local minima. The solution variables from the EJAYA and TLBO optimization algorithms converged to a single point (Fig. 5(e) and (f)), which however does not match the target values.

The same analysis is herein repeated for the SENB test problem (Fig. 7). The PSO algorithm shows a good convergence to the target solution ($E = 1400$ MPa, $G_c = 7.5$ N/mm, $l_c = 1.2$ mm), see Fig. 7(a). The PSO-GA, EJAYA, and the TLBO algorithms converge to points away from the target solution, see Fig. 7(b), (e), and (f). The ABC-PSO and CS algorithms, as in the previous test problem, do not converge, see Fig. 7(c) and (d).

Hence, the above analysis shows that PSO is the most accurate and robust algorithm for phase field fracture mechanics parameters' identification compared to the PSO-GA, ABC-PSO, CS, EJAYA, and TLBO algorithms. This is further observed by the comparison among the simulated force-displacement curves obtained at the end of the execution of each optimization algorithm, where the PSO algorithm accurately matches the target response curve for both virtual test problems, see Fig. 6(a) and (b). The input properties to be determined fall under the category of continuous variable datasets within a user-defined range. The results indicate that the PSO algorithm outperforms PSO-GA for inverse problems when analyzing continuous data variables. Conversely, PSO-GA may be better suited for discrete variable datasets, demonstrating superior performance compared to PSO and other metaheuristic algorithms.

The results are further supported by checking and ensuring that the solution obtained from the PSO algorithm during each optimization iteration is trapped in local minima. The value of the cost function $f(\chi_{\mathbf{opt}})$ during each iteration is calculated from Eq. (13), and it steadily decreases with the number of iterations in both testing problems, see Fig. 8. The plot further confirms the observations on the results plotted in Figs. 5 and 7, showing the difficulty of some meta-heuristic algorithms in reducing the value of the cost function towards zero.

$$f(\chi_{\mathbf{opt}}) = \sqrt{\sum_{d=1}^{n} \left[\frac{\Delta Rx_d(\chi_{\mathbf{opt}})}{Rx_t(\chi_{\mathbf{opt}})} \right]^2} \tag{13}$$

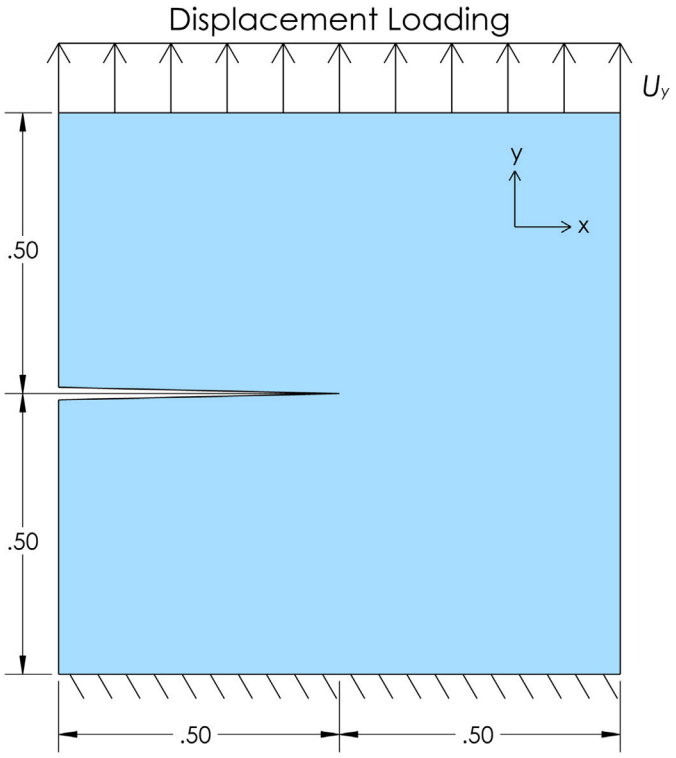

Fig. 3. Geometry and boundary conditions of the tensile test problem for an edge notched specimen (SENT).

A comparative analysis was performed to evaluate the computational runtime and number of iterations required to converge for six evolutionary algorithms, namely PSO, PSO-GA, ABC-PSO, CS, EJAYA, and TLBO. This study was conducted to identify material parameters in phase-field fracture simulations. As evidenced by the results summarized in Table 2, and further supported by the results presented in Figs. 5 and 7, the PSO algorithm consistently demonstrated robust performance, achieving close convergence to the target material parameters in both the SENT and SENB test cases, with the shortest runtime among the successfully converged methods. While PSO-GA and ABC-PSO showed reasonable performance for the SENT problem, only PSO-GA maintained convergence in the SENB case. The CS and ABC-PSO algorithms failed to converge in both test cases, likely due to premature entrapment in local minima. EJAYA and TLBO algorithms converged to suboptimal points, with TLBO exhibiting significantly higher computational time. These results clearly highlight PSO as the most accurate and efficient algorithm for parameter identification in phase-field models of fracture, reinforcing its suitability for practical applications where reliability and computational efficiency are critical. For the reader's reference, all simulations presented in this study were conducted on a dedicated workstation with the following specifications: HP Z2 Mini G3, featuring an Intel(R) Xeon(R) CPU E3-1225 v6 @ 3.30 GHz, 8 GB of RAM, and operating on a 64-bit version of Windows 10 Pro for Workstations.

The above analysis focused on benchmark problems associated with mode-I fractures. Now, we extend the discussion to scenarios involving mixed-mode fracture problems which serve as a benchmark to validate the robustness and accuracy of the PSO-PFF approach under complex loading conditions. The three-point bending unsymmetric configuration in Fig. 9 effectively generates a combination of mode-I and mode-II stress intensities, enabling a comprehensive assessment of the fracture mechanics parameters' prediction capabilities of the method. The geometry of the problem is illustrated in Fig. 9. For the PSO-PFF analysis, the properties to be identified were $E = 1500$ MPa, $G_c = 0.8$ N/mm, $l_c = 1.2$ mm. The constraints and bounds of the design space for the parameters subject to optimization are:

$$\mathscr{X} = \{0.01 < G_c < 2.5 \text{ N/mm};\ 0.6 < l_c < 3.5 \text{ mm};\ 600 < E < 2500 \text{ MPa}\} \tag{14}$$

The evolution of swarm particles within the design space, from their initial positions to their final converged positions, is depicted in Fig. 10. The results demonstrate that the PSO algorithm effectively identifies the optimal particle positions with high accuracy. The convergence behavior of the swarm particles highlights the algorithm's capability to search the design space efficiently, achieving a globally optimized solution while adhering to the defined constraints. To further validate the accuracy of the identified optimum solution, a comparison between the force-displacement curve for the target response and the optimized response is presented in Fig. 11. The close agreement between the target and optimized curves confirms the reliability of the PSO algorithm in capturing the fracture parameters of the mixed-mode fracture problems.

The numerical results obtained for the SENT and SENB benchmark problems (see Figs. 5 and 7) clearly demonstrate that the PSO algorithm provides superior performance in terms of efficiency, robustness, and convergence stability when compared to the hybrid and alternative metaheuristic algorithms considered, namely PSO-GA, ABC-PSO, CS, EJAYA, and TLBO. In particular, the PSO-based identification of phase-field fracture parameters yields more accurate and consistent estimates across different test configurations, thereby validating its suitability as a reliable optimization framework for parameter calibration in phase-field fracture mechanics. Furthermore, the robustness of the PSO framework is not limited to mode-I dominated fracture scenarios; it also extends to mixed-mode fracture conditions. By effectively capturing shear driven crack initiation and propagation, the PSO algorithm demonstrates its ability to identify parameter sets (see Fig. 10) that

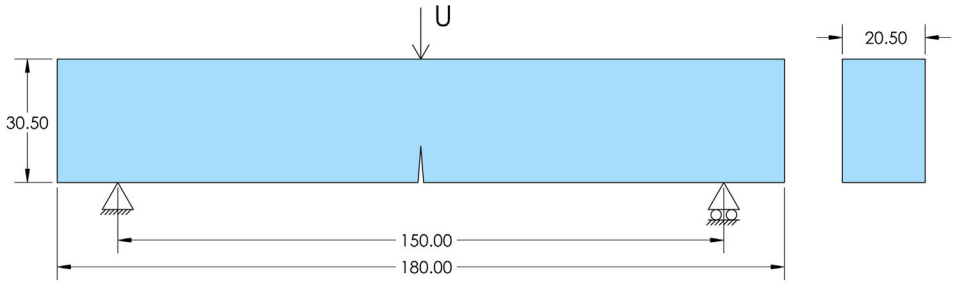

Fig. 4. Geometry and boundary conditions of the SENB test problem.

Table 1
Input data to generate target responses (virtual experiments) and range of parameters for the search space of the identification algorithms.

Test problem	E (GPa)	G_c (N/mm)	l_c (mm)	Range E (GPa)	Range G_c (N/mm)	Range l_c (mm)
SENT test	210	2700	0.3	180–230	1200–3800	0.02–0.45
SENB test	1.4	7.5	1.2	0.9–2.5	1.5–12.5	0.3–3

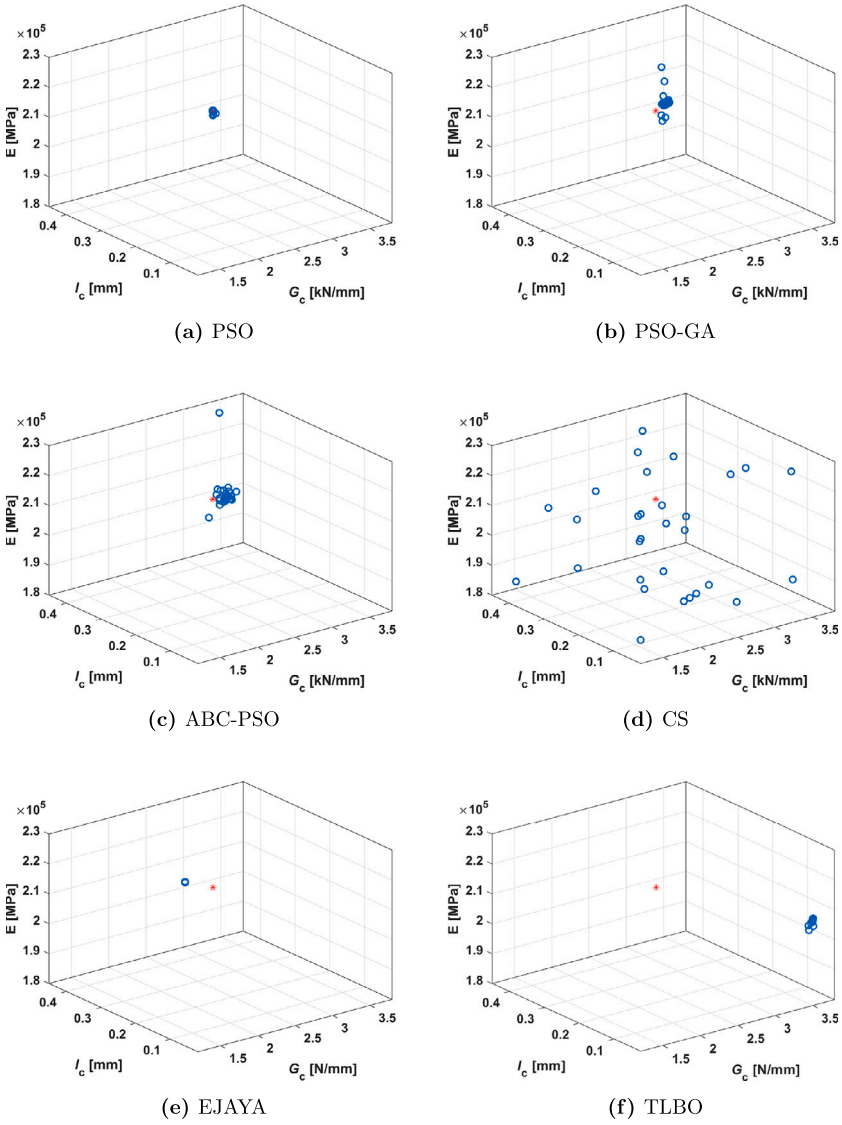

(a) PSO (b) PSO-GA

(c) ABC-PSO (d) CS

(e) EJAYA (f) TLBO

Fig. 5. Comparison of the particles' position predicted by the different optimization algorithms for the tensile test problem with an edge-notched specimen. Not all the algorithms converge to the target response shown with a red star.

govern the complex interplay between normal and tangential separation mechanisms.

Therefore, the PSO algorithm is explored in Section 5.3 to study the influence of anisotropic parameter β in addition to E, G_c, l_c parameters. The proposed methodology is robust and shows promising results for inverse problems nevertheless it has certain limitations. The high computational cost might arise due to the iterative nature of the meta-heuristic algorithms and their sensitivity to initial guess of the solution's design variables which might require optimized tuning of design-constrained space. The risk of convergence to local minima is due to the interdependency of identified fracture parameters and non-convex optimization of search space, which is typical of phase-field problems. Proper setting of the MLA parameters is essential to ensure better algorithm performance. The methodology may be less suitable for inverse problems involving the solution of field variables with a large number of degrees of freedom, as this significantly increases the computational cost. This challenge may be mitigated by leveraging parallel computing techniques or reduced order models to enhance computational efficiency and scalability.

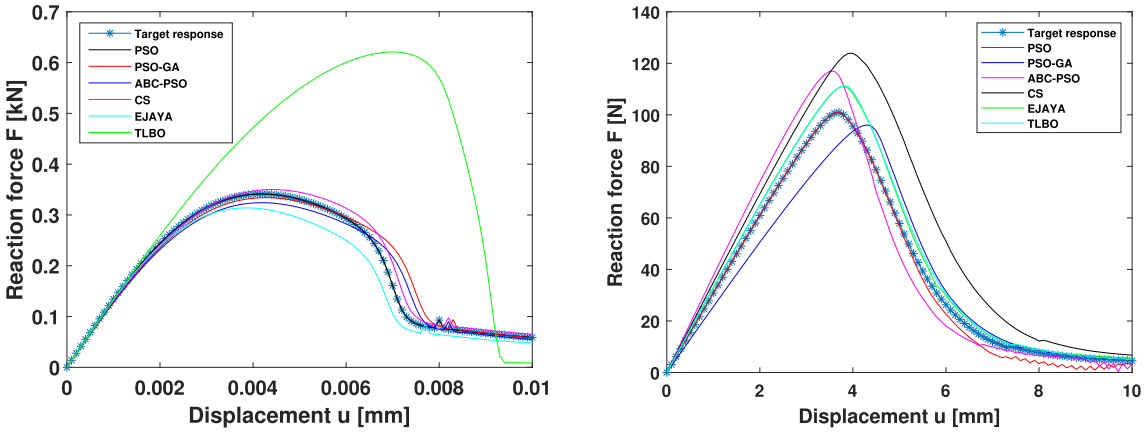

(a) Tensile test with edge-notched specimen (b) SENB test

Fig. 6. Force vs. displacement curves at the end of the execution of the different optimization algorithms; the target response is highlighted by blue stars.

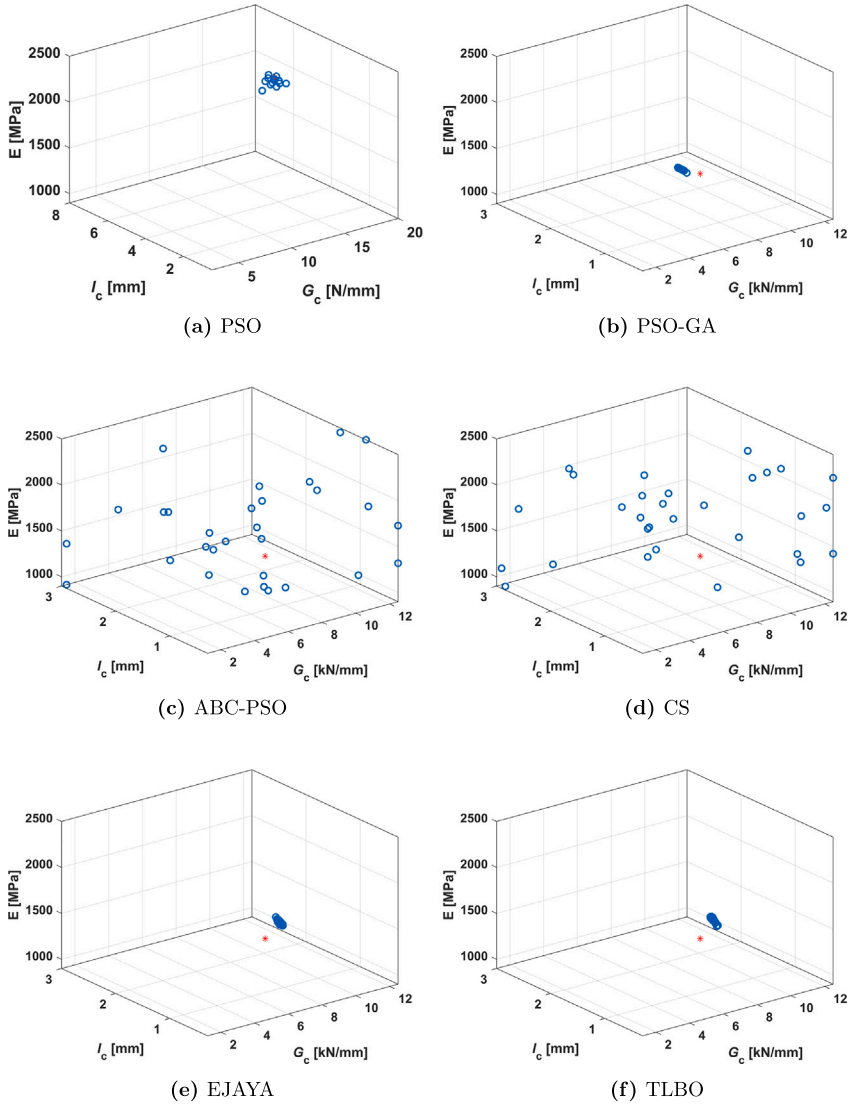

(a) PSO (b) PSO-GA

(c) ABC-PSO (d) CS

(e) EJAYA (f) TLBO

Fig. 7. Comparison of the particles' position predicted by the different optimization algorithms for the SENB test problem. Not all the algorithms converge to the target response shown with a red star.

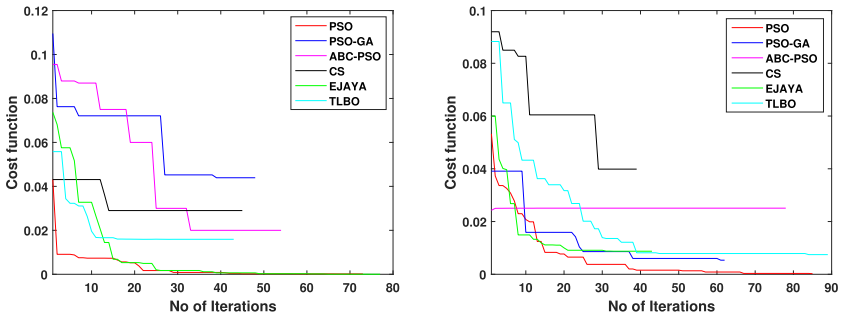

(a) Tensile test with edge-notched specimen (b) SENB test

Fig. 8. Cost function vs. number of iterations for the different meta-heuristic algorithms.

Table 2
Comparison of evolutionary algorithms on benchmark test problems.

Evolutionary Algorithms	SENT (Fig. 3)		SENB (Fig. 4)	
	Run time (hrs)	Number of iterations	Run time (hrs)	Number of iterations
PSO	53.86	41	40.35	38
PSO-GA	87.08	48	67.29	47
ABC-PSO	74.25	44	–	Not converged
CS	–	Not converged	–	Not converged
EJAYA	62.08	39	41.519	42
TLBO	89.58	45	87.35	43

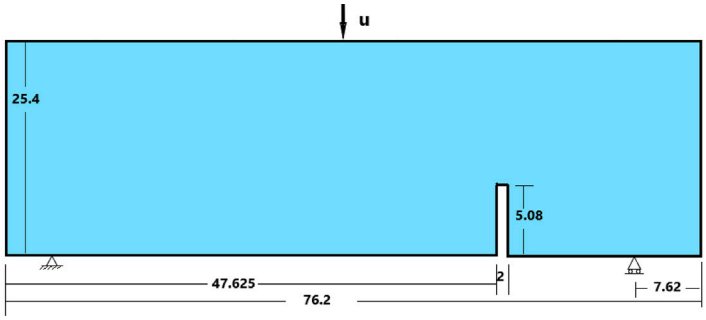

(a) Geometry, dimensions and boundary conditions

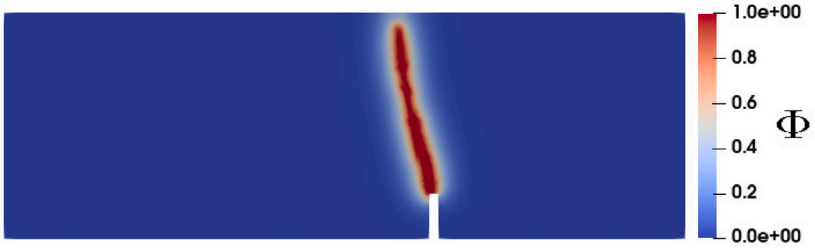

(b) Phase field fracture numerical model prediction

Fig. 9. Three-point bending numerical test case for mixed-mode fracture parameters identification.

5. Application to anisotropic fracture of 3D printed PLA specimens

5.1. Specimens' fabrication process

The PLA specimens to be tested were fabricated via a material extrusion additive manufacturing technique, namely the FDM. First, the specimen geometries for the tensile test (unnotched specimens) and for the SENB testing geometry were designed in SolidWorks 2021, a computer-aided design (CAD) software, see the geometrical data in Fig. 12. The modeled CAD geometry files were exported in STL files and then transferred to the 3D printer DIVIDE_ BY ZERO AION 500 MK2. The G-codes for the FDM printing process were generated using the slicing software - Simplify 3D. The tested specimens were produced from a PLA+ filament spool commercially available (https://esun3dstore.com/).

The PLA filament with an initial diameter of 1.75 mm and density of 1.25 g/cm^3 is hot extruded through a nozzle of 0.6 mm diameter. The extruded filament is deposited layer by layer with respect to material orientation ($\theta = 0°$) onto a pre-heated metallic bed platform by

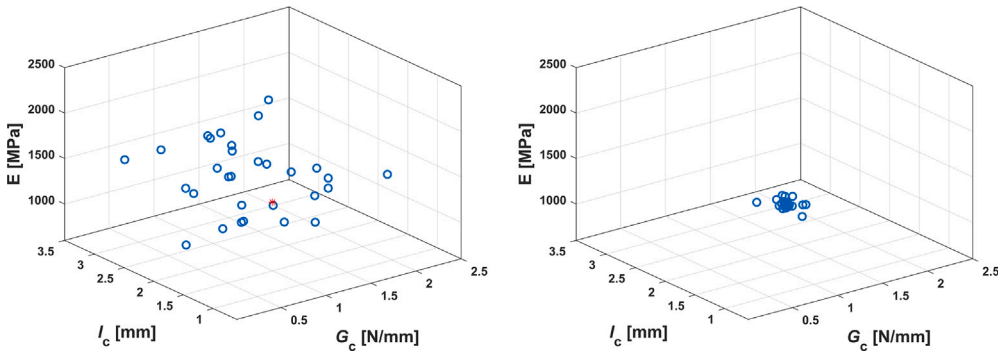

(a) Initial particles' position (b) Final converged particles' position

Fig. 10. Initial and final converged PSO solution for mixed mode fracture problem with target response solution shown with a red star.

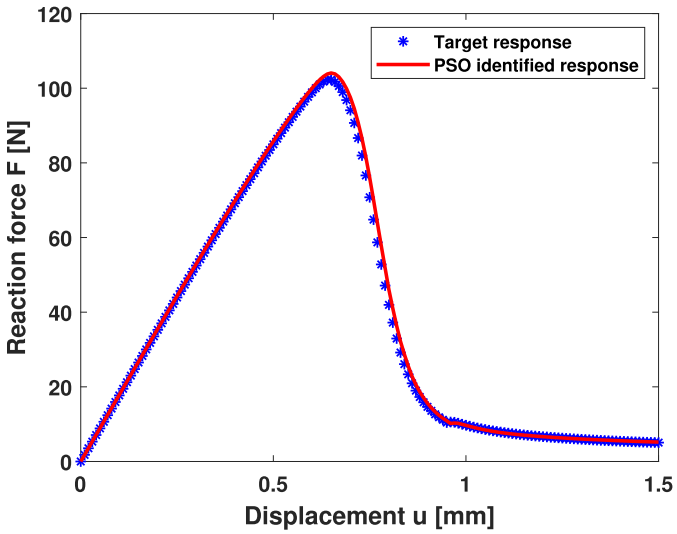

Fig. 11. Force vs. displacement curves of target and PSO identified response for mixed-mode fracture test problem.

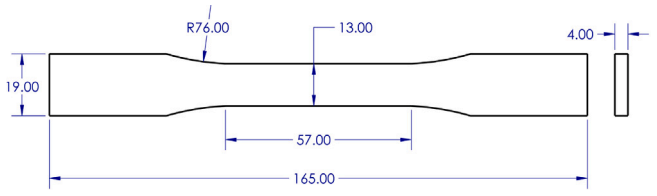

(a) Tensile specimen CAD model

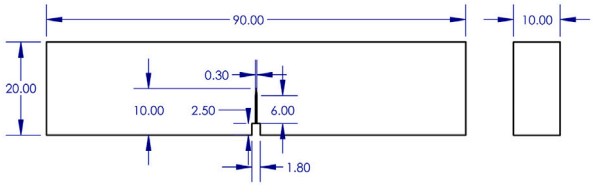

(b) SENB specimen CAD model

Fig. 12. SolidWorks generated CAD geometry models.

following the G-code pattern to obtain the desired geometry. We opted for a 0° material orientation because it maximizes the strength of the 3D-printed material under the selected loading conditions. The 3D printing process parameters to manufacture tensile and SENB specimens made of PLA material have been selected according to the recommendations available in the literature (see Table 3), as it is known that the strength of the tested specimens is greatly influenced by the choice of the printing process parameters [69].

Table 3
Process parameters for the DIVIDE_ BY ZERO AION 500 MK2 3D printer.

Printing process parameters	Values
Nozzle diameter	0.6 mm
Layer height	0.1 mm
Infill pattern	Aligned
Infill density	100 %
Pattern rotation	0°
Nozzle temperature	200 °C
Bed temperature	65 °C
Printing speed	70 mm/s
Travel speed	90 mm/s
Filament diameter	1.75 mm

5.2. Experimental characterization and the issue of epistemic uncertainty

The tensile and SENB specimens were manufactured with a 0° material orientation and according to the ASTM D638 [24] and ASTM D5045-14 [26] standards, respectively, as shown in Fig. 13. Ten replicas of tensile and SENB specimens were mechanically tested up to failure using the Tinius Olsen universal testing machine with a 10 kN load cell capacity. In all the tests, a crosshead displacement rate of 3 mm/min was imposed. The Young's modulus E and the tensile strength $\sigma_{\max}$ were collected from the tensile tests, and the data are reported with their mean and standard deviations in Table 4. The obtained mean value of the Young's modulus, 1067.2 MPa, is lower than that reported in previous publications [12,20,22]. A possible reason might be related to the effect of different printing process parameters [30,69]. On the other hand, the mean value of the tensile strength, 43.1 MPa, is within the range reported in the previous literature. The stress-strain curves for the ten tensile samples are shown in Fig. 14: the specimen breaks almost when it reaches the tensile strength, with no sign of plastic yielding and a very brittle behavior, which justifies the application of the phase field approach to fracture for brittle materials.

The experimental setup for the SENB tests followed the ASTM D5045-14 standards. The dimensions of the manufactured SENB specimens were set accordingly. Therefore, the fracture toughness K_{IC} ($\mathrm{MPa}\sqrt{\mathrm{m}}$) was determined by meeting the requirements in Eqs. (15a) and (15b):

(a) Dog bone specimens for the tensile tests (b) SENB specimens

Fig. 13. Photos of the 3D printed PLA specimens.

Table 4
Experimental data obtained by processing the tensile and the SENB tests of 3D printed PLA material.

Specimen No.	Tensile tests		SENB tests		
	E (MPa)	σ_{max} (MPa)	P_{max} (N)	K_{IC} (MPa$\sqrt{m}$)	G_{IC} (N/mm)
1	1194.39	38.5	946	7.12	41.39
2	1175.31	46.2	826	6.22	31.56
3	1129.08	39.3	929	7.00	39.92
4	1072.68	46.1	893	6.72	36.88
5	1059.94	46.2	915	6.89	38.72
6	1003.52	43.9	1170	8.81	63.32
7	965.47	44.1	1200	9.04	66.60
8	994.12	40.0	1040	7.83	50.03
9	1060.68	42.5	1100	8.28	55.97
10	1016.81	44.2	965	7.52	43.07
Mean	1067.20	43.1	998	7.54	46.75
Std. dev.	77.53	2.92	124	0.93	11.77

$$(W - a_c) > 2.5\left(\frac{K_{IC}}{\sigma_{max}}\right)^2 \tag{15a}$$

$$0.45 < \frac{a_c}{W} < 0.55 \tag{15b}$$

where B and W represent the specimen thickness and height equal to 10 mm and 20 mm, respectively; a_c is the pre-crack length equal to 10 mm; σ_{max} is the maximum tensile stress at failure estimated from tensile tests, and K_{IC} is the plane-strain fracture toughness of the material. The pre-notch in the specimens was manufactured during the 3D printing process, to minimize potential imperfections and variations in the value of this parameter.

The SENB tests were performed, and the maximum load (P_{max}) at failure for each specimen was recorded; see Table 4. The fracture toughness K_{IC} was determined according to [26] based on Eq. (16) for all the SENB specimens and results are reported in Table 4 with values in the range of $[6-9]$ MPa$\sqrt{m}$.

$$K_{IC} = \frac{P_{max}}{B\sqrt{W}} f\left(\frac{a_c}{W}\right) \tag{16}$$

where the function f for $0 < a_c/W < 1$ reads:

$$f\left(\frac{a_c}{W}\right) = 6\left(\frac{a_c}{W}\right)^{1/2} \times \left\{ \frac{1.99 - \frac{a_c}{W}\left[1 - \left(\frac{a_c}{W}\right)\right]\left[2.15 - 3.93\left(\frac{a_c}{W}\right) + 2.7\left(\frac{a_c}{W}\right)^2\right]}{\left[1 + 2\left(\frac{a_c}{W}\right)\right]\left[1 - \left(\frac{a_c}{W}\right)\right]^{3/2}} \right\} \tag{17}$$

In this work, the relationship between fracture toughness K_{IC} and fracture energy G_{IC} is considered under plane strain conditions, as fracture toughness represents a true material property only in this regime. The experimental tests were conducted in accordance with ASTM D5045-14 [26], which specifies specimen geometries that ensure valid plane strain fracture toughness measurements. Consequently, the experimentally obtained K_{IC} values can be consistently converted into G_{IC} and implemented within the phase-field framework to achieve reliable numerical predictions of fracture behavior. The relationship between fracture toughness K_{IC} and fracture energy G_{IC} for plane strain

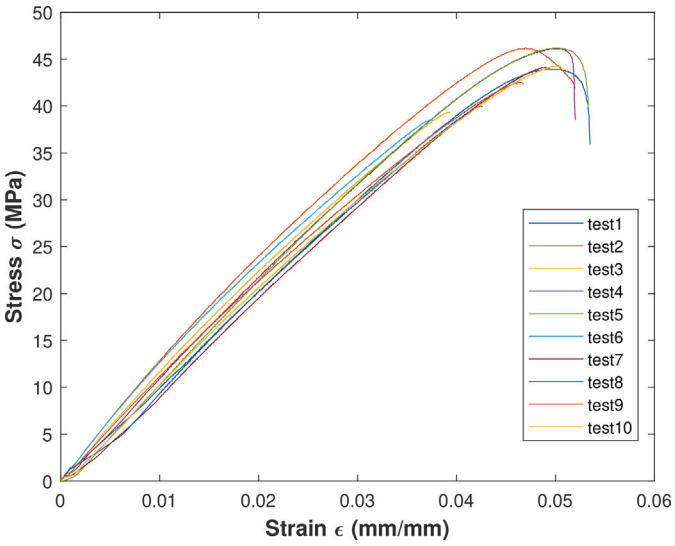

Fig. 14. Experimental stress-strain curves from tensile tests.

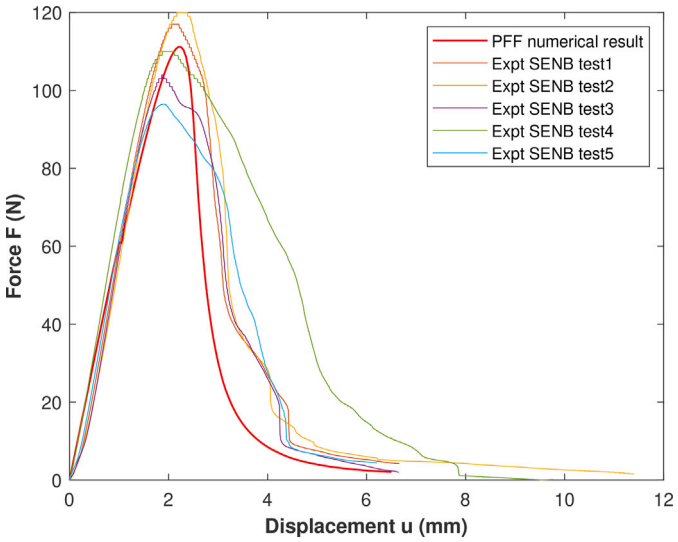

Fig. 15. Comparison of numerical and experimental Force–Displacement responses for SENB test on 3D-Printed PLA.

conditions is calculated from Ref. [70]:

$$G_{\mathrm{IC}} = \frac{K_{\mathrm{IC}}^2(1-\nu^2)}{E} \tag{18}$$

where E and ν are the Young's modulus and the Poisson's ratio of the material, respectively. To calculate G_{IC} values for SENB specimens, the mean value of $E = 1067.2$ MPa obtained from the tensile tests was considered, and $\nu = 0.36$ was also determined from uniaxial tensile tests and is consistent with the literature. The calculated G_{IC} values are reported in Table 4.

A direct comparison between the numerical simulations and experimental results for the SENB tests is presented in Fig. 15, focusing on the global force–displacement response. The phase-field model demonstrates a reasonable ability to replicate the average experimental trend using a set of fracture parameters defined by $G_c = 12$ N/mm and $l_c = 2.5$ mm. It is important to note that the fracture energy adopted in the numerical model is lower than the experimentally determined value of $G_c = 46.75$ N/mm. This difference might be caused by additional energy dissipation mechanisms occurring in the experiments, such as plastic deformation, interfacial debonding, and crazing, which are not accounted for in the present model, and pose further challenges for reliability studies and epistemic uncertainty quantification. Despite the model simplification, the numerical results exhibit good qualitative agreement with the experimental data, supporting the robustness of the phase-field approach in capturing the overall fracture response of 3D-printed PLA under mode-I loading conditions.

In this study, the elastic response of the material is modeled as isotropic, whereas anisotropy is introduced solely in the fracture energy contribution. This assumption is justified on the basis that the dominant source of anisotropy in 3D-printed materials often manifests more strongly in their fracture resistance (due to layer-by-layer bonding, print path orientation, and interfacial defects) than in their bulk elastic stiffness, which may remain approximately isotropic when homogenized at the macroscale. By assuming isotropic elasticity, the mechanical equilibrium problem is simplified, and the directional dependence of crack evolution is isolated within the phase-field fracture term. If elastic anisotropy were considered, the governing equations would require the use of a fully anisotropic stiffness tensor with additional calibration parameters, leading to increased computational cost and potential ambiguity in separating the contributions of elastic versus fracture anisotropy. Therefore, the present isotropic elasticity assumption is consistent with the goal of highlighting fracture anisotropy effects, while retaining a computationally efficient model.

In addition, it is essential to emphasize the role of parameter identification and sensitivity analysis in validating the assumptions of the proposed phase-field fracture framework when applied to real case studies. The accuracy of the predictions is highly dependent on the correct estimation of the elastic modulus E, which governs the material's load-bearing stiffness; the critical energy release rate G_c, which characterizes the fracture resistance; the length scale parameter l_c, which controls the width of the diffused crack and thereby the resolution of crack localization; and the anisotropy parameter β, which affects the degree and orientation of directional crack propagation. Careful calibration of these parameters against experimental data ensures that the model not only reproduces the global force–displacement behavior but also the observed fracture patterns. Sensitivity analysis further highlights the interdependence of these parameters. Identifying the relative influence of each parameter is crucial to distinguish whether variations in fracture response stem from elastic assumptions (isotropy vs. anisotropy) or from the fracture-related anisotropy. This analysis not only supports the present modeling assumption of isotropic elasticity with anisotropic fracture, but also pinpoints the possibility to apply identification algorithms to make an insight into epistemic uncertainty quantification, which is an issue inherent to any material model.

5.3. Application of the PFF-MLA approach for parameter identification and sensitivity analysis

The phase-field fracture parameters are herein identified according to the proposed PFF-MLA procedure in case of an anisotropic fracture model, see Section 3. The results in Section 3 evidenced that particle

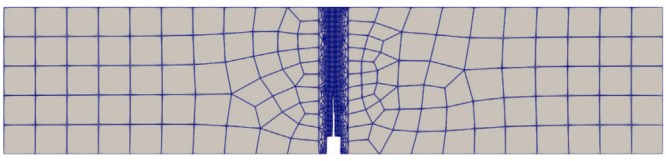

Fig. 16. Finite element mesh of the simulated SENB tests.

Table 5
Set of input data to generate target responses and range of parameters for the sensitivity analysis of the anisotropic fracture tensor.

Fixed parameter	E (MPa)	G_c (N/mm)	l_c (mm)	β	Range E (GPa)	Range G_c (N/mm)	Range l_c (mm)	Range β
G_C	2500	12	2.5	25	900–2500	–	0.5–8	5–100
l_c	2500	12	2.5	25	900–2500	2.5-20	–	5–100
E	2500	12	2.5	25	–	2.5–20	0.5–8	5–100
β	2500	12	2.5	25	900–2500	2.5–20	0.5–8	–

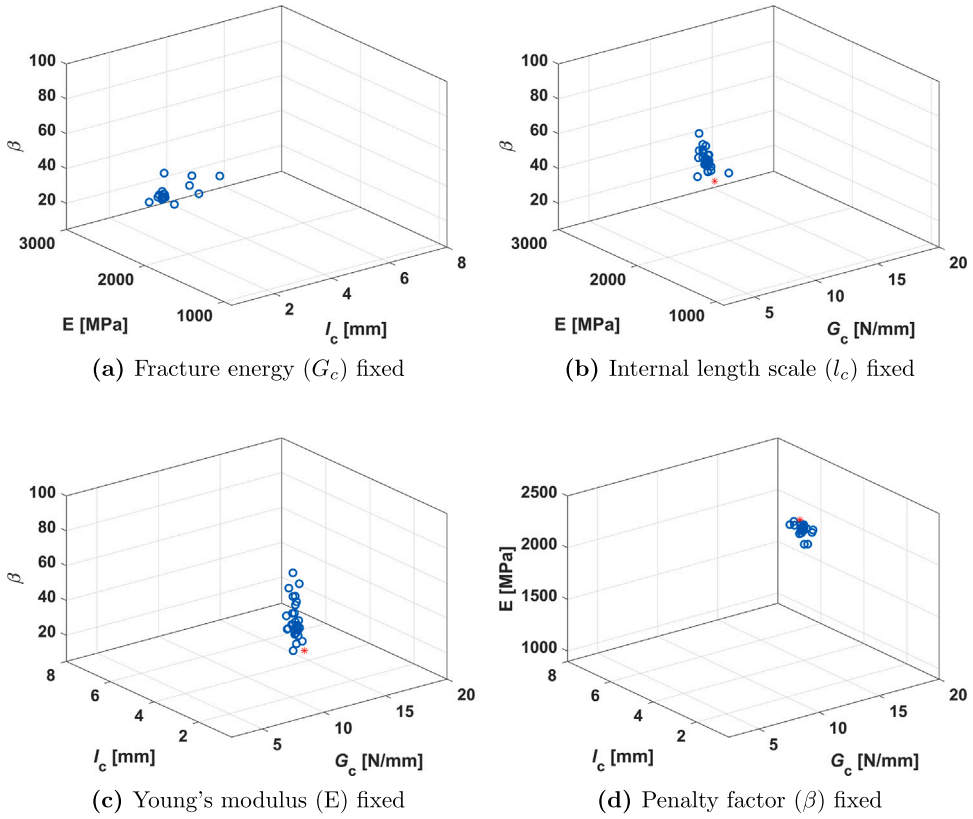

(a) Fracture energy (G_c) fixed (b) Internal length scale (l_c) fixed

(c) Young's modulus (E) fixed (d) Penalty factor (β) fixed

Fig. 17. Sensitivity analysis of anisotropic phase-field fracture parameters.

swarm optimization (PSO) outperformed the other metaheuristic algorithms and, therefore, is herein used. The FE mesh of the CAD model shown in Fig. 13(b) was created using the software Gmsh [71], see Fig. 16. Plane strain conditions are assumed with a fine discretization along the potential direction of crack growth and a total of 1751 finite elements in the model.

The phase field model for anisotropic fracture is implemented into a fully integrated four-node quadrilateral element as a user element in the MATLAB software DAEDALON [72]. The model parameters considered for the initial study of sensitivity analysis were $G_c = 12$ N/mm, $l_c = 2.5$ mm, $E = 2500$ MPa, $\beta = 25$. The design-constrained solution space of the problem is given in Eq. (19).

$$\mathscr{X} = \{2.5 < G_c < 20 \text{ N/mm}; 0.5 < l_c < 8 \text{ mm}; \times 900 < E < 3000 \text{ MPa}; 5 < \beta < 100\} \tag{19}$$

Preliminary investigation suggests that all the four design variables (G_c, l_c, E, β) would not converge to the required target solution ($G_c = 12$ N/mm, $l_c = 2.5$ mm, $E = 2500$ MPa, $\beta = 25$) when simultaneously identified. Therefore, it is proposed to investigate the effect of three design parameters by fixing the fourth parameter as shown in Table 5 with the parameter space in Eq. (19). The optimization simulation results for four cases mentioned in Table 5 are shown in Fig. 17, which illustrates the convergence behavior of the parameter optimization process under different parameter-fixing strategies. Fig. 17 reveals that, by fixing G_c or β, the results converge to the target solution (see Fig. 17(a) and (d)). In contrast, by fixing l_c and E, the results do not converge to the target solution as shown in Fig. 17(b) and (c), respectively. Hence, the focus initially shifts to the penalty parameter β in conducting sensitivity analysis. This examination aims to understand the influence of β on determining fracture mechanics parameters within the anisotropic PFF numerical model. In the context of phase-field modeling for anisotropic fracture, several researchers [34,35,41,42,73,74] have focused on β rather than G_c and have made diverse choices regarding the value of β in relation to the constraint on crack orientation along the fracture plane. While the authors have not explicitly discussed the rationale behind the choice of β value, it is evident that selecting an appropriate value for the penalty parameter β is crucial to represent the behavior of anisotropic materials during fracture processes and accurately predict the force-displacement curve. Consequently, the study investigates how varying the penalty parameter β impacts the results of fracture energy (G_c) and peak force ($P_{\max}$) values.

For sensitivity analysis, the FE model as shown in Fig. 16 is explored and PPF FEA is carried out for different β values ranging from $\{0-100\}$ as shown in Table 6 and compared with the isotropic case $\beta = 0$ and

Table 6
Sensitivity analysis of β and percentage (%) change in P_{max}, G_c values for different values of β with respect to $\theta = 0°$, $\beta = 0$.

Penalty parameter β	% change with respect to $\theta = 0°, \beta = 0$	
0	–	–
0.5	0	0
5	19.97	28.46
10	28.02	44.11
15	32.29	53.65
20	34.99	60.22
25	36.86	65.08
30	38.27	68.84
35	39.36	71.87
40	40.21	74.39
45	40.96	76.49
50	41.57	78.31
55	42.09	79.89
60	42.56	81.30
65	42.97	82.54
70	43.32	83.65
75	43.64	84.69
80	43.95	85.63
85	44.23	86.48
90	44.48	87.28
95	44.71	88.03
100	44.92	88.72

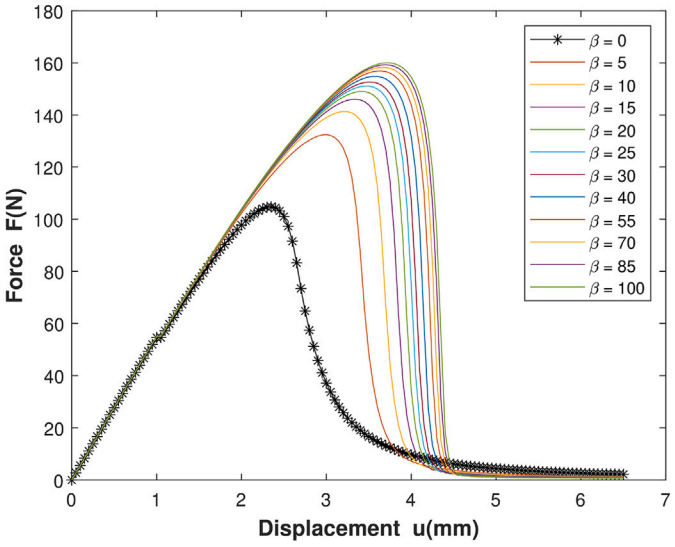

Fig. 18. Force - displacement curve for $\theta = 0°$, and different β values.

material orientation $\theta = 0°$. The percentage (%) change in peak force (P_{max}) and fracture energy (G_c) values for different β values with respect to case ($\theta = 0°$, $\beta = 0$) as reported in Table 6 confirms that there is a significant influence of $\beta \in \{0 - 40\}$ on the results, while the impact is negligible with $\beta \in \{45 - 100\}$. This result is clearly visible in the force-displacement curves plotted for different β values, as shown in Fig. 18. In this study, the penalty parameter β was varied within the range $\beta \in [0, 100]$ to investigate its influence on the peak force (P_{max}) and fracture energy (G_c). The chosen interval is consistent with values reported in the phase-field fracture literature, where moderate β values ensure stable and accurate capture of anisotropic effects without inducing numerical ill-conditioning. A negative value of β would mathematically imply a reduction of fracture resistance in certain orientations, which is non-physical and may lead to unstable or unrealistic solutions (e.g., negative dissipation or spurious crack growth). Therefore, the admissible range of β is restricted to non-negative values. Beyond $\beta = 100$, preliminary simulations confirmed that the results converge and exhibit negligible variation, justifying the upper bound of the sensitivity analysis.

Table 7
Showing test cases involving varying crack density functions with and without the application of a correction factor for conducting PFF numerical tests ($\theta = 0°, \beta = 25$).

	Crack density function	r value
test 1	Anisotropic crack density function correction	4
test 2	Anisotropic crack density function correction	2
test 3	Anisotropic crack density function correction	4/3
test 4	Anisotropic crack density function without correction	–
test 5	Isotropic crack density function ($\beta = 0$)	–

The above sensitivity analysis is a result of incorporating the penalty parameter β, which aids in tracking the crack path along material orientation planes θ. By increasing the fracture energy G_c along preferential crack path directions, the penalty parameter β also enhances the value of the peak force. Therefore, it is advisable to adjust the values of G_c and l_c when employing an anisotropic phase field fracture model to improve the prediction of crack path direction and force-displacement curve. In [42], efforts were made to correct the values of G_c and l_c (see Eq. (20) where $r = 4$) in Eq. (8) to maintain the ratio G_c/l_c unchanged, ensuring the physical value of G_c remains consistent within the fracture plane:

$$G_{cc} = \frac{G_c}{\sqrt[r]{1+\beta}}, \quad l_{cc} = \frac{l_c}{\sqrt[r]{1+\beta}} \tag{20}$$

This prompts the question of whether these corrected values of G_c and l_c can be generalized to any geometry, boundary and loading conditions. The investigation was conducted to validate findings by examining single edge notch tensile and bending test scenarios, as depicted in Figs. 3 and 4 of Section 4, utilizing identical material properties as input conditions. Numerical tests were executed for various crack surface density functions ($\theta = 0°, \beta = 25$), as outlined in Table 7. The force-displacement plots for both numerical problems are shown in Fig. 19. Tests 1 through 4 were compared with test 5 (refer to Table 7), revealing from Fig. 19 that the anisotropic crack density function, with or without correction factor, does not align with the isotropic case. In both test problems (see Fig. 19(a) and (b)), the force-displacement results for $r = 2$ and 4/3 underestimate the peak force, while for $r = 4$, test 4 overestimates the peak force compared to the isotropic case.

Now we deal with the SENB testing problem with dimensions of 90 mm × 20 mm, as illustrated in Fig. 20, meshed with 108 × 24 square finite elements. Material properties selected for analysis were $G_c = 12$ N/mm, $l_c = 2.5$ mm, $E = 2500$ MPa, $\beta = 25$. The pre-notch was introduced by imposing Dirichlet boundary conditions ($\Phi = 1$, depicted in red in Fig. 20). Numerical analysis was conducted for all test cases listed in Table 7. Results indicate that for $r = 2$ in Eq. (20), the force-displacement curve (see Fig. 21) closely aligns with the isotropic crack density function while retaining the physical value of G_c. Discrepancies in peak force predictions for other cases (e.g., $r = 4$ and 4/3) suggest that the effectiveness of these corrections is not entirely geometry independent. These findings indicate that although the correction factor strategy is formulated generically, its practical performance is influenced by the specific boundary conditions, loading modes, and geometry. These observations emphasize the need for further validation across a broader range of geometries, boundary conditions, and loading scenarios to fully generalize the proposed correction strategy. Further investigation into anisotropic phase-field fracture models is particularly essential to ensure accurate prediction of crack trajectories and force–displacement responses, while preserving the physical value of the fracture energy parameter G_c.

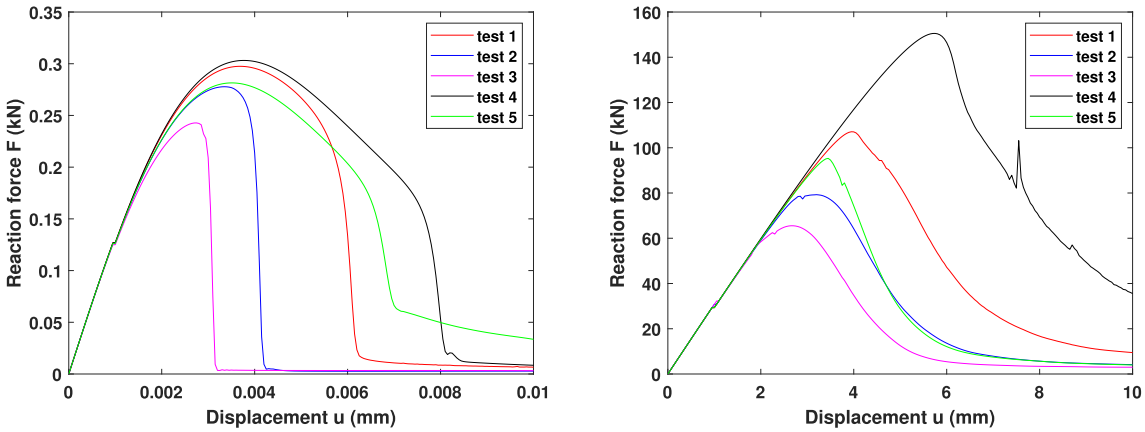

(a) single edge notch tensile test (b) single edge notch bending test

Fig. 19. Force vs. displacement curves for different test cases ($\theta = 0°, \beta = 25$) as mentioned in Table 7.

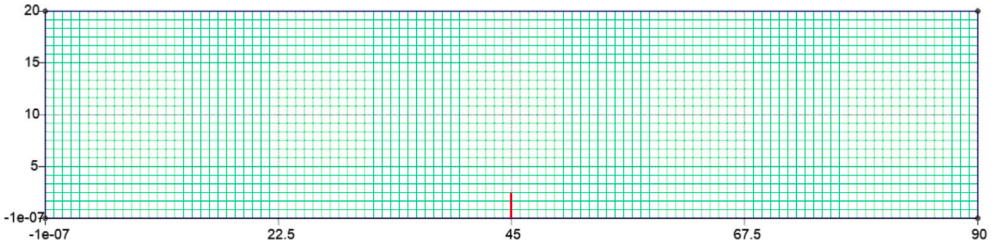

Fig. 20. SENB geometric model with meshing details for case $\theta = 0°$, $\beta = 25$.

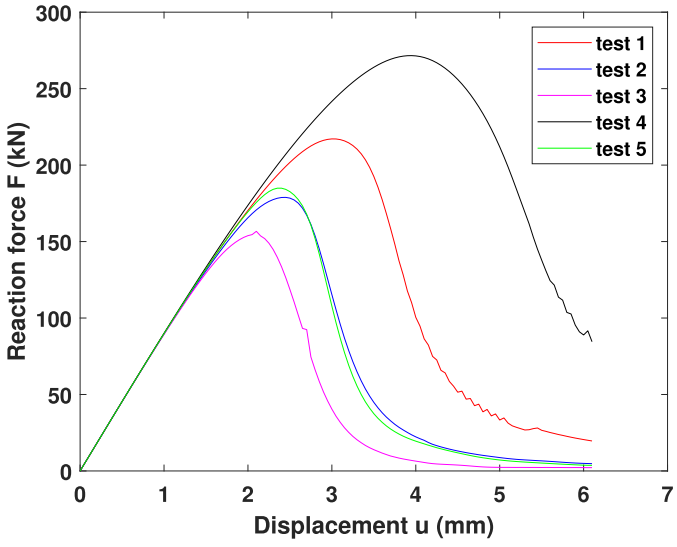

Fig. 21. Force-displacement curve for SENB numerical problem (see Fig. 20) for case $\theta = 0°$, $\beta = 25$.

6. Conclusion

In this work, we proposed the combined PFF-MLA approach to tackle inverse problems and identify the phase field fracture parameters. The metaheuristic machine learning algorithms (MLA) like PSO, PSO-GA, ABC-PSO, CS, TLBO, and EJAYA algorithms have been compared to identify the best parametric analysis optimization algorithm. SENT and SENB test problems were chosen for the analysis considering the isotropic case $\beta = 0$. Results report that particle swarm optimization (PSO) is more efficient and robust in identifying fracture mechanics parameters than PSO-GA, ABC-PSO, CS, TLBO, and EJAYA. Therefore, the sensitivity analysis of the fracture mechanics parameters has been carried out using the PFF-PSO MLA considering different model assumptions to get an insight into the epistemic uncertainty of the phase field approach to fracture when applied to 3D printed isotropic or anisotropic materials, since different model assumptions can be put forward in terms of elastic properties and fracture energy. In the anisotropic case ($\beta \neq 0$), the critical fracture energy release rate G_c to be used in the model is overestimated. Also, the peak force is increased due to the influence of the penalty parameter β. The sensitivity analysis reports that the anisotropic phase field for fracture has to be further scrutinized for better quantitative predictions, in addition to qualitative analysis of the crack path.

Regarding the experimental analysis of 3D-printed PLA material, the study was limited to reporting material properties: Young's modulus (E) and tensile strength ($\sigma_{\max}$) from tensile tests, and fracture energy properties K_{IC}, G_{IC} from single edge notch bending tests. The results were reported following ASTM standards. Future research aims at investigating and simulating the experimental force-displacement response curve with the anisotropic phase field fracture model, tracking the crack path qualitatively without compromising the quantitative results, and for different material orientations.

The results of this study demonstrated that evolutionary algorithms can effectively identify optimal parameters for phase-field fracture models, and can be a tool for assessing model uncertainties when applied to real materials. This capability holds significant potential for real-world applications, where accurate modeling of fracture behavior is critical. By enabling reliable calibration of model parameters such as fracture energy G_c and the length scale parameter l_c, the proposed approach supports the design of materials with enhanced fracture resistance. Furthermore, it can improve the predictive capabilities of computational fracture simulations used in structural health monitoring, failure analysis, and safety assessment of critical components in aerospace, marine, and civil engineering industries.

CRediT authorship contribution statement

Tota Rakesh Kumar: Writing – review & editing, Writing – original draft, Visualization, Validation, Software, Methodology, Investigation, Formal analysis, Data curation, Conceptualization. **Marco Paggi:** Writing – review & editing, Methodology, Supervision, Investigation, Conceptualization.

Declaration of competing interest

The authors declare that they have no known competing financial interests or personal relationships that could have appeared to influence the work reported in this paper.

Data availability

Data may be provided upon request.

References

[1] Vafadar A, Guzzomi F, Rassau A, Hayward K. Advances in metal additive manufacturing: a review of common processes, industrial applications, and current challenges. Appl Sci 2021;11(3):1213. https://doi.org/10.3390/app11031213

[2] Dogea R, Yan XT, Millar R. Additive manufacturing process design for complex aircraft components. Int J Adv Manuf Technol 2022;123(11):4195–211. https://doi.org/10.1007/s00170-022-10413-x

[3] Jandyal A, Chaturvedi I, Wazir I, Raina A, Haq MIU. 3D printing–a review of processes, materials and applications in Industry 4.0. Sustain Oper Comput 2022;3:33–42. https://doi.org/10.1016/j.susoc.2021.09.004

[4] Zhang J, Song B, Wei Q, Bourell D, Shi Y. A review of selective laser melting of aluminum alloys: processing, microstructure, property and developing trends. J Mater Sci Technol 2019;35(2):270–84. https://doi.org/10.1016/j.jmst.2018.09.004

[5] Delgado J, Serenó L, Monroy K, Ciurana J. Selective laser sintering. Mod Manuf Process 2019:481–99. https://doi.org/10.1002/9781119120384.ch20

[6] Shaqour B, Abuabiah M, Abdel-Fattah S, Juaidi A, Abdallah R, Abuzaina W, Qarout M, Verleije B, Cos P. Gaining a better understanding of the extrusion process in fused filament fabrication 3D printing: a review. Int J Adv Manuf Technol 2021;114:1279–91.

[7] Rajan K, Samykano M, Kadirgama K, Harun WSW, Rahman MM. Fused deposition modeling: process, materials, parameters, properties, and applications. Int J Adv Manuf Technol 2022;120(3):1531–70. https://doi.org/10.1007/s00170-022-08860-7

[8] Ahn D-G. Directed energy deposition (DED) process: state of the art. Int J Precis Eng Manuf-Green Technol 2021;8:703–42. https://doi.org/10.1007/s40684-020-00302-7

[9] Singh S, Ramakrishna S, Berto F. 3D printing of polymer composites: a short review. Mater Des Process Commun 2020;2(2):e97. https://doi.org/10.1002/mdp2.97

[10] Sharma A, Rai A. Fused deposition modelling (FDM) based 3D & 4D printing: a state of art review. Mater Today Proc 2022;62:367–72. https://doi.org/10.1016/j.matpr.2022.03.679

[11] Kumaresan R, Samykano M, Kadirgama K, Pandey AK, Rahman MM. Effects of printing parameters on the mechanical characteristics and mathematical modeling of FDM-printed PETG. Int J Adv Manuf Technol 2023;128(7–8):3471–89. https://doi.org/10.1007/s00170-023-12155-w

[12] Marşavina L, Vălean C, Mărghitaş M, Linul E, Razavi N, Berto F, Brighenti R. Effect of the manufacturing parameters on the tensile and fracture properties of FDM 3D-printed PLA specimens. Engng Fract Mech 2022;274:108766. https://doi.org/10.1016/j.engfracmech.2022.108766

[13] Felfel RM, Hossain KMZ, Parsons AJ, Rudd CD, Ahmed I. Accelerated in vitro degradation properties of polylactic acid/phosphate glass fibre composites. J Mater Sci 2015;50:3942–55. https://doi.org/10.1007/s10853-015-8946-8

[14] Elsawy MA, Kim K-H, Park J-W, Deep A. Hydrolytic degradation of polylactic acid (PLA) and its composites. Renew Sustain Energy Rev 2017;79:1346–52. https://doi.org/10.1016/j.rser.2017.05.143

[15] Nagarajan V, Mohanty AK, Misra M. Perspective on polylactic acid (PLA) based sustainable materials for durable applications: focus on toughness and heat resistance. ACS Sustain Chem Eng 2016;4(6):2899–916. https://doi.org/10.1021/acssuschemeng.6b00321

[16] Zohoor S, Abolfathi N, Solati-Hashjin M. Accelerated degradation mechanism and mechanical behavior of 3D-printed PLA scaffolds for bone regeneration. Iran Polym J 2023;32(10):1209–27. https://doi.org/10.1007/s13726-023-01191-8

[17] Feng P, Jia J, Liu M, Peng S, Zhao Z, Shuai C. Degradation mechanisms and acceleration strategies of poly (lactic acid) scaffold for bone regeneration. Mater Des 2021;210:110066. https://doi.org/10.1016/j.matdes.2021.110066

[18] Sharifi J, Rizvi G, Fayazfar HR. Sustainable 3D printing of enhanced carbon nanotube-based polymeric nanocomposites: green solvent-based casting for eco-friendly electrochemical sensing applications. Int J Adv Manuf Technol 2024:1–13. https://doi.org/10.1007/s00170-024-13337-w

[19] Chacón JM, Caminero MA, García-Plaza E, Núnez PJ. Additive manufacturing of PLA structures using fused deposition modelling: effect of process parameters on mechanical properties and their optimal selection. Mater Des 2017;124:143–57. https://doi.org/10.1016/j.matdes.2017.03.065

[20] Zhao Y, Chen Y, Zhou Y. Novel mechanical models of tensile strength and elastic property of FDM AM PLA materials: experimental and theoretical analyses. Mater Des 2019;181:108089. https://doi.org/10.1016/j.matdes.2019.108089

[21] Alvarez-Blanco M, Arias-Blanco A, Infante-García D, Marco M, Giner E, Miguélez MH. Influence of material extrusion parameters on fracture mechanisms of polylactic acid under three-point bending. Engng Fract Mech 2023;283:109223. https://doi.org/10.1016/j.engfracmech.2023.109223

[22] Wang S, Ma Y, Deng Z, Zhang S, Cai J. Effects of fused deposition modeling process parameters on tensile, dynamic mechanical properties of 3D printed polylactic acid materials. Polymer Test 2020;86:106483. https://doi.org/10.1016/j.polymertesting.2020.106483

[23] Zou R, Xia Y, Liu S, Hu P, Hou W, Hu Q, Shan C. Isotropic and anisotropic elasticity and yielding of 3D printed material. Compos Part B Eng 2016;99:506–13. https://doi.org/10.1016/j.compositesb.2016.06.009

[24] ASTM International. Standard test method for tensile properties of plastics, 2014. https://doi.org/10.1520/D0638-14

[25] Song Y, Li Y, Song W, Yee K, Lee K-Y, Tagarielli VL. Measurements of the mechanical response of unidirectional 3D-printed PLA. Mater Des 2017;123:154–64. https://doi.org/10.1016/j.matdes.2017.03.051

[26] Inernational ASTM. Standard test methods for plane-strain fracture toughness and strain energy release rate of plastic materials. ASTM D5045-99 2007. https://doi.org/10.1520/D5045-14

[27] McLouth TD, Severino JV, Adams PM, Patel DN, Zaldivar RJ. The impact of print orientation and raster pattern on fracture toughness in additively manufactured ABS. Addit Manuf 2017;18:103–9. https://doi.org/10.1016/j.addma.2017.09.003

[28] Hart KR, Wetzel ED. Fracture behavior of additively manufactured acrylonitrile butadiene styrene (ABS) materials. Engng Fract Mech 2017;177:1–13. https://doi.org/10.1016/j.engfracmech.2017.03.028

[29] Es-Said OS, Foyos J, Noorani R, Mendelson M, Marloth R, Pregger BA. Effect of layer orientation on mechanical properties of rapid prototyped samples. Mater Manuf Process 2000;15(1):107–22. https://doi.org/10.1080/10426910008912976

[30] Lay M, Thajudin NLN, Hamid ZAA, Rusli A, Abdullah MK, Shuib RK. Comparison of physical and mechanical properties of PLA, ABS and nylon 6 fabricated using fused deposition modeling and injection molding. Compos Part B Eng 2019;176:107341. https://doi.org/10.1016/j.compositesb.2019.107341

[31] Miehe C, Hofacker M, Welschinger F. A phase field model for rate-independent crack propagation: robust algorithmic implementation based on operator splits. Comput Methods Appl Mech Eng 2010;199(45–48):2765–78. https://doi.org/10.1016/j.cma.2010.04.011

[32] Francfort GA, Marigo J-J. Revisiting brittle fracture as an energy minimization problem. J Mech Phys Solids 1998;46(8):1319–42. https://doi.org/10.1016/S0022-5096(98)00034-9

[33] Griffith AA. Vi. The phenomena of rupture and flow in solids. Philos Trans R Soc Lond Ser A Contain Pap Math Phys Character 1921;221(582–593):163–98. https://doi.org/10.1098/rsta.1921.0006

[34] Clayton JD, Knap JJCMS. Phase field modeling of directional fracture in anisotropic polycrystals. Comput Mater Sci 2015;98:158–69. https://doi.org/10.1016/j.commatsci.2014.11.009

[35] Teichtmeister S, Kienle D, Aldakheel F, Keip M-A. Phase field modeling of fracture in anisotropic brittle solids. Int J Non-Linear Mech 2017;97:1–21. https://doi.org/10.1016/j.ijnonlinmec.2017.06.018

[36] Li B, Maurini C. Crack kinking in a variational phase-field model of brittle fracture with strongly anisotropic surface energy. J Mech Phys Solids 2019;125:502–22. https://doi.org/10.1016/j.jmps.2019.01.010

[37] Bijaya A, Sagar S, Chowdhury SR. A consistent multi-phase-field formulation for anisotropic brittle fracture. Engng Fract Mech 2024;295:109825. https://doi.org/10.1016/j.engfracmech.2023.109825

[38] Li W, Li P, Nguyen-Thanh N, Zhou K. A hybrid thermo-mechanical phase-field model for anisotropic brittle fracture. Engng Fract Mech 2024:110219. https://doi.org/10.1016/j.engfracmech.2024.110219

[39] Nguyen-Thanh N, Rabczuk T. Phase-field modeling of anisotropic crack propagation based on higher-order nonlocal operator theory. Int J Solids Struct 2024;289:112632. https://doi.org/10.1016/j.ijsolstr.2023.112632

[40] Nguyen-Thanh N, Nguyen-Xuan H, Li W. Phase-field modeling of anisotropic brittle fracture in rock-like materials and polycrystalline materials. Comput Struct 2024;296:107325. https://doi.org/10.1016/j.compstruc.2024.107325

[41] Nguyen T-T, Réthoré J, Yvonnet J, Baietto M-C. Multi-phase-field modeling of anisotropic crack propagation for polycrystalline materials. Computational Mech 2017;60:289–314. https://doi.org/10.1007/s00466-017-1409-0

[42] Riad S, Bardel D, Réthoré J. Unified phase field model to simulate both intergranular and transgranular failure in polycrystalline aggregates. Finite Elem Anal Des 2021;194:103555. https://doi.org/10.1016/j.finel.2021.103555

[43] Kennedy J, Eberhart R. Particle swarm optimization. In: Proceedings of ICNN'95-international conference on neural networks, vol. 4. 1995. p. 1942–8. https://doi.org/10.1109/ICNN.1995.488968

[44] Tota RK, Paggi M. A robust identification procedure for phase field fracture mechanics parameters. Theor Appl Fract Mech 2023;127:104005. https://doi.org/10.1016/j.tafmec.2023.104005

[45] Carollo V, Piga D, Borri C, Paggi M. Identification of elasto-plastic and nonlinear fracture mechanics parameters of silver-plated copper busbars for photovoltaics. Engng Fract Mech 2019;205:439–54. https://doi.org/10.1016/j.engfracmech.2018.11.014

[46] Wu T, Rosić B, De Lorenzis L, Matthies HG. Parameter identification for phase-field modeling of fracture: a Bayesian approach with sampling-free update. Computational Mech 2021;67:435–53. https://doi.org/10.1007/s00466-020-01942-x

[47] Eberhart RC, Shi Y. Comparing inertia weights and constriction factors in particle swarm optimization. In: Proceedings of the 2000 Congress on Evolutionary Computation. CEC00 (Cat. No. 00th8512), vol. 1. 2000. p. 84–8. https://doi.org/10.1109/CEC.2000.870279
[48] Zhang Q, Ogren RM, Kong S-C. A comparative study of biodiesel engine performance optimization using enhanced hybrid PSO–GA and basic GA. Appl Energy 2016;165:676–84. https://doi.org/10.1016/j.apenergy.2015.12.044
[49] El-Abd M. A hybrid ABC-SPSO algorithm for continuous function optimization. In: 2011 IEEE symposium on swarm intelligence; 2011. p. 1–6. https://doi.org/10.1109/SIS.2011.5952576
[50] Li Z, Wang W, Yan Y, Li Z. Ps–abc: a hybrid algorithm based on particle swarm and artificial bee colony for high-dimensional optimization problems. Expert Syst Appl 2015;42(22):8881–95. https://doi.org/10.1016/j.eswa.2015.07.043
[51] Salgotra R, Singh U, Saha S. New cuckoo search algorithms with enhanced exploration and exploitation properties. Expert Syst Appl 2018;95:384–420. https://doi.org/10.1016/j.eswa.2017.11.044
[52] Rao RV, Kalyankar VD. Parameter optimization of modern machining processes using teaching–learning-based optimization algorithm. Eng Appl Artif Intell 2013;26(1):524–31. https://doi.org/10.1016/j.engappai.2012.06.007
[53] Zhang Y, Chi A, Mirjalili S. Enhanced jaya algorithm: a simple but efficient optimization method for constrained engineering design problems. Knowl Based Syst 2021;233:107555. https://doi.org/10.1016/j.knosys.2021.107555
[54] Zitar RA, Al-Betar MA, Awadallah MA, Doush IA, Assaleh K. An intensive and comprehensive overview of Jaya algorithm, its versions and applications. Arch Comput Methods Eng 2022;29(2):763–92. https://doi.org/10.1007/s11831-021-09585-8
[55] Bourdin B, Francfort GA, Marigo J-J. The variational approach to fracture. J Elast 2008;91:5–148. https://doi.org/10.1007/s10659-007-9107-3
[56] Wu J-Y. A unified phase-field theory for the mechanics of damage and quasi-brittle failure. J Mech Phys Solids 2017;103:72–99. https://doi.org/10.1016/j.jmps.2017.03.015
[57] Braides A. Approximation of free-discontinuity problems, no. 1694, Springer; 1998. https://doi.org/10.1007/BFb0097344
[58] Burke S, Ortner C, Süli E. An adaptive finite element approximation of a generalized Ambrosio–Tortorelli functional. Math Models Methods Appl Sci 2013;23(9):1663–97. https://doi.org/10.1142/S021820251350019X
[59] Bourdin B, Francfort GA, Marigo J-J. Numerical experiments in revisited brittle fracture. J Mech Phys Solids 2000;48(4):797–826. https://doi.org/10.1016/S0022-5096(99)00028-9
[60] Abdel-Basset M, Abdel-Fatah L, Sangaiah AK. Metaheuristic algorithms: a comprehensive review. Comput Intell Multimed Big Data Cloud Eng Appl 2018:185–231. https://doi.org/10.1016/B978-0-12-813314-9.00010-4
[61] Yang X-S. Nature-inspired metaheuristic algorithms. Luniver Press; 2010.
[62] Gandomi AH, Yang X-S, Talatahari S, Alavi AH. Metaheuristic algorithms in modeling and optimization. Metaheuristic Applications in Structures and Infrastructures 2013;1:1–24.
[63] Clerc M. The swarm and the queen: towards a deterministic and adaptive particle swarm optimization. In: Proceedings of the 1999 Congress on Evolutionary Computation-CEC99 (Cat. No. 99th8406), vol. 3. 1999. p. 1951–7. https://doi.org/10.1109/CEC.1999.785513
[64] Sivanandam SN, Deepa SN, Sivanandam SN, Deepa SN. Genetic Algorithms. Springer; 2008. https://doi.org/10.1007/978-3-540-73190-0_2
[65] Karaboga D, Basturk B. A powerful and efficient algorithm for numerical function optimization: artificial bee colony (ABC) algorithm. J Glob Optim 2007;39:459–71. https://doi.org/10.1007/s10898-007-9149-x
[66] Rao RV, Rao RV. Teaching-Learning-Based Optimization Algorithm. Springer; 2016. https://doi.org/10.1007/978-3-319-22732-0_2
[67] Rao RV, Patel V. An improved teaching-learning-based optimization algorithm for solving unconstrained optimization problems. Scientia Iranica 2013;20(3):710–20. https://doi.org/10.1016/j.scient.2012.12.005
[68] Rao R. Jaya: a simple and new optimization algorithm for solving constrained and unconstrained optimization problems. Int J Ind Eng Comput 2016;7(1):19–34. https://doi.org/10.5267/j.ijiec.2015.8.004
[69] Mohamed OA, Masood SH, Bhowmik JL. Optimization of fused deposition modeling process parameters: a review of current research and future prospects. Adv Manuf 2015;3:42–53. https://doi.org/10.1007/s40436-014-0097-7
[70] Irwin GR. Analysis of stresses and strains near the end of a crack traversing a plate 1957. https://doi.org/10.1115/1.4011547
[71] Geuzaine C, Remacle J-F. Gmsh: a 3-D finite element mesh generator with built-in pre-and post-processing facilities. Int J Numer Methods Eng 2009;79(11):1309–31. https://doi.org/10.1002/nme.2579
[72] Baaser H. Development and application of the finite element method based on Matlab. Springer; 2010. https://doi.org/10.1007/978-3-642-13153-0
[73] Natarajan S, Annabattula RK, et al. Modeling crack propagation in variable stiffness composite laminates using the phase field method. Compos Struct 2019;209:424–33. https://doi.org/10.1016/j.compstruct.2018.10.083
[74] Nguyen TT, Réthoré J, Baietto M-C. Phase field modelling of anisotropic crack propagation. Eur J Mech A Solids 2017;65:279–88. https://doi.org/10.1016/j.euromechsol.2017.05.002